



Mohammad Javad Pour Razzaghi · Cheng Xu · Aliakbar Emamverdian

The interaction of vortices induced by a pair of microjets in the turbulent boundary layer

Received: 15 April 2021 / Revised: 23 September 2021 / Accepted: 24 September 2021 / Published online: 28 October 2021
© The Visualization Society of Japan 2021

Abstract Experimental and numerical study of active and passive flow control are notable and highly practical subjects in aircraft and missiles. Fluid jets are invaluable tools for this purpose. Accordingly, the present study delves into the effects of a pair of air microjets on turbulent flow over a plate. For this purpose, numerical model results were verified by experimental data of flow over a plate in the presence of a pair of air jets. Next, vortex formation, merging, and dissipation into the flow were studied at velocity ratio, $VR = 4.0$, by changing the spacing between the pair of jets and their orientations. The vortex position relative to the floor and other vortices, vortex intensity, flow velocity, Reynolds stresses in different directions, and pressure are discussed. The best vortex-merging results were found in a pair of co-directional jets ($d/D = 10$) condition. A pair of co-directional jets ($d/D = 10$) produced better results than opposite ones ($d/D = 10 - ccr$). In the configuration with $d/D = 10$, the vortex intensity was nearly 80% higher than that of the single jet case. Further, the pair of jets pushed the post-jet pressure rise around 30 cm away.

Keywords Pair of micro-jets · Turbulent boundary layer · Vortex formation · Merging vorticities · Longitudinal vortex dissipation · Numerical solution

1 Introduction

An adverse pressure gradient develops with the rise of static pressure along the stream. The adverse pressure gradient disturbs the velocity profile in the boundary layer. Granted the adverse pressure gradient is large enough, it can induce a backflow toward upstream, separating the boundary layer from the surface. This phenomenon creates promoting drag over the surface. The resulting flow separation can be delayed through active and passive control methods. In the passive method, energy is injected into the boundary layer through the main stream. Meanwhile, in the active control method, energy is supplied by an external source (Lefebvre 2015; Anderson 2001; Failed 2016). Vortex generator jets (VGJs) are examples of active control and can be placed in the stream individually or in an array. This method is similar to using vane vortex generators (VVGs) (Pearcey 1961). The main advantage of using VGJs over VVGs is that jets can be integrated actively into the system. Further, jets do not exacerbate the drag exerted on the system. Nonetheless, using VVGs in numerical and experimental solutions is more time and resource-consuming than VGJs (PourRazzaghi and Xu 1507). Moreover, instead of a single jet, an array of jets can be used to boost the vortex forming in the flow and extend the effects further into the flow. In the case of a jet configuration, the turbulent boundary layer evolves according to the skew angle of the jets' direction as longitudinal vortices merge or move independently. As mentioned earlier, the effects of a single jet and arrays of jets on the boundary layer have been addressed in several experimental and numerical work

studies. McCurdy is possibly the first to have studied the effects of vortex generators on controlling the airfoil boundary layer in 1948 (McCurdy 1948). In 1952, Wallis studied the effects of inclined VGJs and VVGs. According to this work, jet arrays exert similar effects to vanes on the flow (Wallis 1952). In 1961, Pearcey was the first to study the effects of VGJs and VVGs on boundary layer separation control (Pearcey 1961). Rixon and Johari showed that the circulation and maximum vortex intensity diminish exponentially by moving away from the jet. Further, by increasing the jet-to-fluid-velocity ratio, the distance to the point of vortex formation increases relatively linearly (Rixon and Johari 2003). In 2007, Ortmanns and Kähler studied the jet effects on the shear layer and the turbulence properties of the boundary layer. Their studies concluded that the VGJ has partial effects on turbulent kinetic energy (Ortmanns and Kähler 2007). In an experimental study (2006), Godard and Stanislas investigated the effects of the fluid jet on the skin friction of a plate placed in the wind tunnel. They offer a quantitative comparison between three passive, slotted, and round-jet vortex generators. Further, the study investigates the effects of co-rotating and counter-rotating jets, suggesting that the former type produces better results (Godard and Stanislas 2006). In 2012, Von Stillfried et al. experimentally studied VGJs for boundary layer control. The study used a pair or an array of jets placed transversally to the flow. They considered such parameters as jet spacing and jet angle. According to their results, in pairs, the VGJs exert slightly more influence over the flow than in the single configuration, but the results were mostly similar (Stillfried et al. 2012). Feng et al. studied an inclined jet trajectory model with incompressible cross-flow in 2017. Further, jet entrainment, horseshoe vortices, and wake vortices that may create a low-pressure region over the wall, changing the jet trajectory and affecting jet rotation, were discussed at low VR and skew angles close to 90° (Feng et al. 2018). In an experimental study (2018), Beresh et al. investigated the velocity field effects on pressure distribution over the surface in a cross-flow with jets and vanes. It was found that a pair of counter-rotating vortices formed when the stream passes over a vertical jet. Also, pressure fluctuations are principally driven by the jet wake deficit and the wall horseshoe vortex. In addition, the inclined nozzle produces a vortex pair. This vortex pair impinges the fin and yields stronger pressure fluctuations driven more directly by turbulence emanating from the jet mixing (Beresh et al. 2018). Alimi and Wunsch investigated active flow control of canonical laminar separation bubbles by steady and harmonic vortex generator jets using direct numerical simulations in 2018. According to these results, disturbances caused by VGJs make the large-scale coherent structures. So the separated region is limited due to the effect of these structures at increasing the momentum exchange (Alimi and Wunsch 2018). Liu and et al. used the compression corner calculation model and conducted detailed numerical investigations in the supersonic flow field in 2019. They studied the effects of different injection pressure ratios, various actuation positions, and different nozzle types. Moreover, they mentioned that the distance between the counter-rotating vortex pair and the wall surface is an important factor (Liu et al. 2019). Wang and Ghaemi studied the effects of vane sweep angle on the vortex generator wake in 2019. Their experimental studies compared the stream flowing over a pair of deltas, trapezoidal, and rectangular vanes. They also discussed such parameters as vortex spacing, intensity, and turbulence (Wang and Ghaemi 2019). But there are still fewer studies on minute vortex generator jets (micro-VGJs) and the interaction of vortices induced by microjets up to now.

With all that said, the present study relies on a numerical solution method to investigate the effects of 1 mm minute jet pairs placed at different relative distances on turbulent flow over a plate. For this purpose, co-directional and opposite jet pairs were compared in terms of vortex intensity, merging, and stability. We have also comprehensively discussed the vortex position relative to the boundary layer and its formation and dissipation. Velocity and Reynolds stress were the other topics addressed.

Figure 1 depicts the wind tunnel model geometry. The figure shows the geometry dimensions and boundary conditions. The model dimensions in the x and z directions were 3.5 and 0.5 m, respectively. The values of y at the inlet and outlet ends of the tunnel were 0.13 and 0.231 m, respectively. The microjet was located 1.13 m from the inlet of the tunnel. It was 0.001 m in diameter. Further, this problem considers a pair of transversally-positioned jets. The configuration was investigated with the jets spaced at $d/D = 10$ and 30. Moreover, the angles were set at $\alpha = 30^\circ$ and $\beta = 60^\circ$ for co-directional jets and $\beta = -60^\circ$ and 60° for opposite jets. The jets were placed symmetrically on the two sides of the $z = 0$ line. The fluid considered was the air with viscosity $\mu = 1.81 \times 10^{-5}$ kg/sm and density $\rho = 1.12$ kg/m³. The inflow velocity was 15.0 m/s, and its turbulence intensity was 2%. The ratio of turbulent to molecular viscosity at the inlet and outlet boundaries was set to 5% and 10%, respectively. Table 1 presents the geometrical definitions of the problem as well as its inputs and outputs.

Table 1 Parameters definitions and values

Parameter	Definition	Parameter	Definition
U	Velocity in the x -direction	$L = 3.5$ m	Total surface length
V	Velocity in the y -direction	$d = 0.001$ m	Microjet diameter
W	Velocity in the z -direction	$D = 10\text{--}30$ d	Distance between microjets
$U = 15$ m/s	Inflow velocity	$h = 0.005$ m	Distance of the microjet from the center of the surface
u'	Speed fluctuation in the x direction	$\alpha = 30$	Pitch angle of jet hole
v'	Speed fluctuation in the y direction	$\beta = 60^\circ, -60^\circ$	Skew angle of the jet hole relative to x -direction
w'	Speed fluctuation in the z direction	δ	Boundary layer thickness
$V_{jet} = 15, 30,$ and 60 m/s	Fluid microjet velocity	$\rho = 1.12$ kg/m ³	Fluid density
ω_x	Vorticity in the x direction	$\mu = 1.81 \times 10^{-5}$ kg/sm	Fluid viscosity
Y^+	A measure of the application range of wall functions	IT = 2%	Turbulence intensity
		$\mu_t/\mu = 5\% - 10\%$	The ratio of turbulent to molecular viscosity

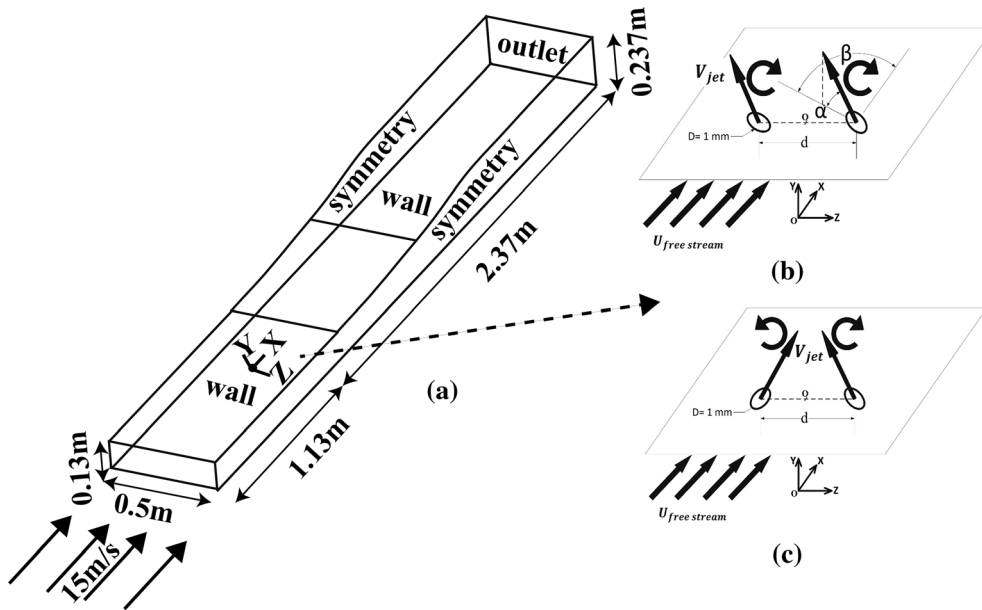


Fig. 1 Dimensions and boundary conditions of the computational domain: **a** All the domain, **b** Co-rotational pair jets, and **c** Counter co-rotational pair jets

2 Modeling and governing equations

Figure 1 depicts the wind tunnel model geometry. The figure shows the geometry dimensions and boundary conditions. The model dimensions in the x - and z -directions were 3.5 and 0.5 m, respectively. The values of y at the inlet and outlet ends of the tunnel were 0.13 and 0.231 m, respectively. The microjet was located 1.13 m from the inlet of the tunnel. It was 0.001 m in diameter. Further, this problem considers a pair of transversally-positioned jets. The configuration was investigated with the jets spaced at $d/D = 10$ and 30. Moreover, the angles were set at $\alpha = 30^\circ$ and $\beta = 60^\circ$ for co-directional jets and $\beta = -60^\circ$ and 60° for opposite jets. The jets were placed symmetrically on the two sides of the $z = 0$ line. The fluid considered was the air with viscosity $\mu = 1.81 \times 10^{-5}$ kg/sm and density $\rho = 1.12$ kg/m³. The inflow velocity was 15.0 m/s, and its turbulence intensity was 2%. The ratio of turbulent to molecular viscosity at the inlet and outlet boundaries was set to 5% and 10%, respectively. Table 1 presents the geometrical definitions of the problem as well as its inputs and outputs.

Navier–stokes equations were expanded to RANS turbulent models and solved numerically for flow analysis. The finite volume method was employed for the numerical analysis of these equations in the

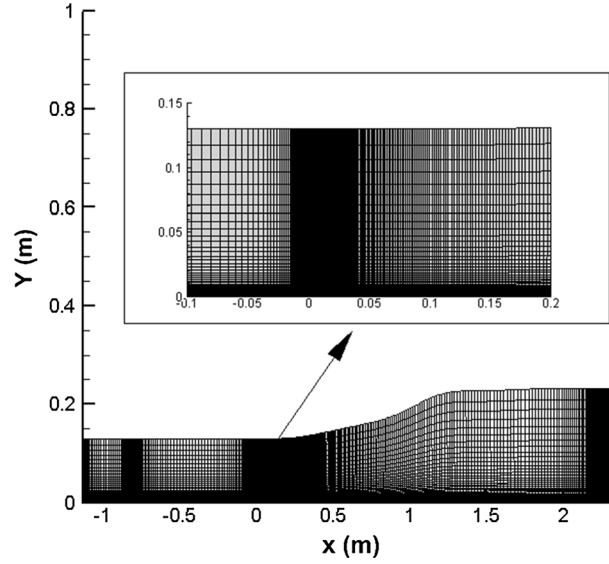


Fig. 2 The mesh file used for the computational domain

computational domain. Further, pressure and momentum equations were expanded by the second-order upwind scheme, coupling velocity and pressure fields by the SIMPLE algorithm.

So, to solve the RANS equations, the continuity and momentum equations in incompressible flow are used as in Eqs. 1 and 2, respectively (Masumi and Nikseresht 2017):

$$\text{div}(\vec{v}) = \nabla \cdot \vec{v} = 0.0 \quad (1)$$

$$\frac{\partial \vec{V}}{\partial t} + (\nabla \cdot \vec{V}) \vec{V} = \frac{1}{\rho} \nabla \cdot \sigma + \vec{g} \quad (2)$$

where σ is stress tensor and is equal to:

$$\sigma_{ij} = -p\delta_{ij} + 2(\mu + \mu_t)S_{ij} \quad (3)$$

where p, S, μ, V, ρ , and δ_{ij} are static pressure, strain tensor rate, dynamic viscosity, fluid velocity, fluid density, and Kronecker delta function, respectively. Also, μ_t is turbulence viscosity which should be calculated with the SST K- ω model.

It is worth noting that the parameter $\nu_t = \mu_t/\rho$, representing dynamic viscosity, was calculated through SST K- ω . Within the SST K- ω model, the transfer equations for turbulence kinetic energy and specific dissipation rate were solved coupled with the equations above. Here, G_k is the turbulence kinetic energy generated due to average velocity gradients, and G_ω is the generated specific dissipation rate. Γ_k and Γ_ω denote the diffusion effects of k and ω , respectively, whereas Y_k and Y_ω represent dissipations of k and ω , respectively. D_ω represents cross-diffusion, and S_k and S_ω are sources defined by the user (White and Majdalani 2006; Davidson 2015).

$$\frac{\partial(\rho k)}{\partial t} + \frac{\partial(\rho k u_i)}{\partial x_i} = \frac{\partial}{\partial x_j} \left(\Gamma_k \frac{\partial(k)}{\partial x_j} \right) + G_k + Y_k + S_k \quad (4)$$

$$\frac{\partial(\rho \omega)}{\partial t} + \frac{\partial(\rho \omega u_i)}{\partial x_i} = \frac{\partial}{\partial x_j} \left(\Gamma_\omega \frac{\partial(\omega)}{\partial x_j} \right) + G_\omega + Y_\omega + D_\omega + S_\omega \quad (5)$$

Resulting from flow velocity fluctuation terms, Reynolds stresses were modeled by considering turbulent viscosity. For incompressible flows, Reynolds stresses were calculated as follows.

$$-\rho \overline{u'_i u'_j} = \mu_t \left(\frac{\partial \overline{u}_i}{\partial x_j} + \frac{\partial \overline{u}_j}{\partial x_i} \right) - \frac{2}{3} \rho k \delta_{ij} \quad (6)$$

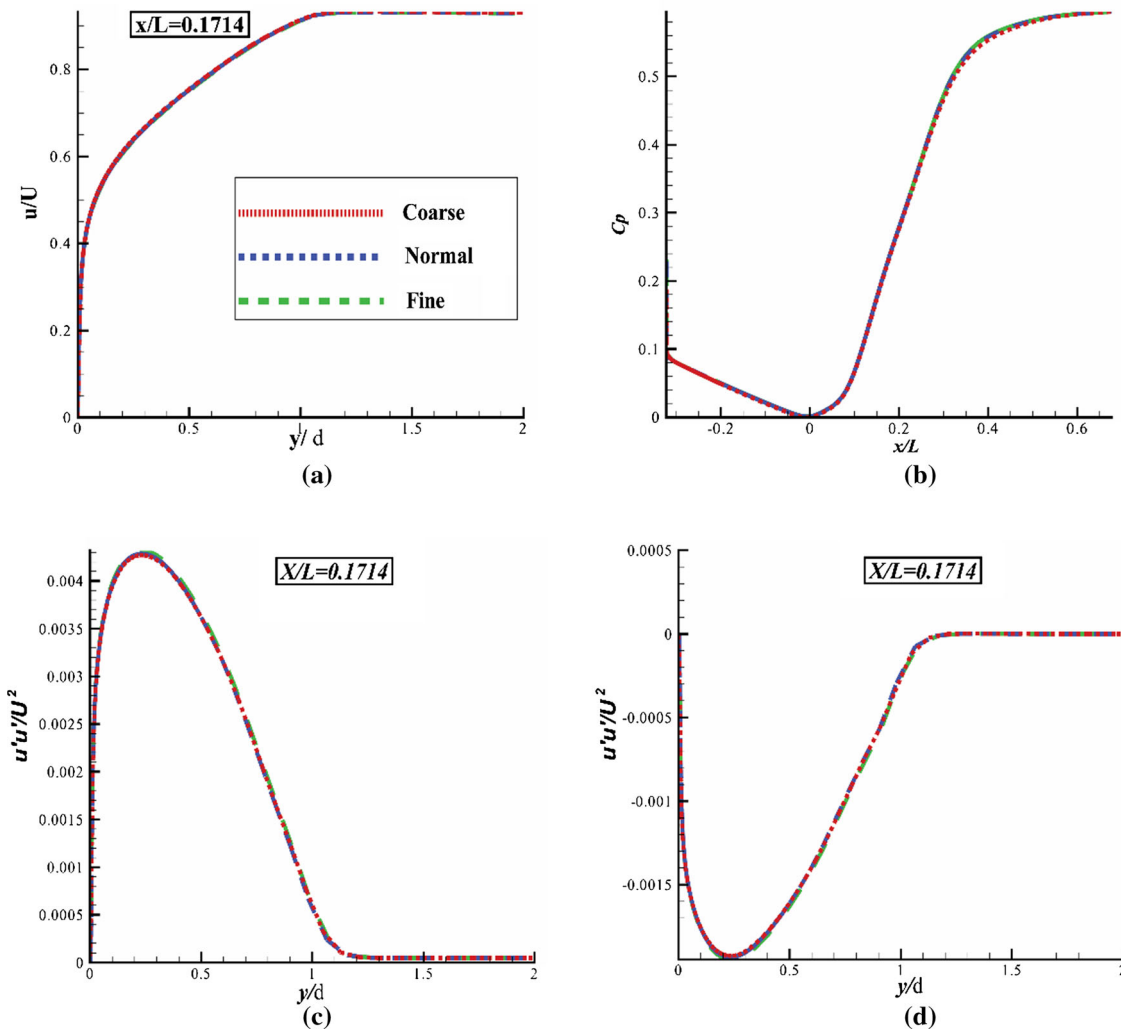


Fig. 3 Results for mesh independency: a u/U , b C_p at the lower wall, c $u'u'/U^2$, and d $u'v'/U^2$

3 Verification

The present study investigates the effects of a VGJ pair on the turbulent boundary layer over a plate. For this purpose, after studying grid independence, model results were compared to experimental results for configurations with jets. Then, after proving the numerical model's accuracy, the results were studied under different conditions.

Figure 2 depicts the present geometry, for which a HEX mesh is used for grid generation. The mesh is finer in regions with more important and intensified flow variations such as near the VGJs, the lower, and the inlet boundaries of the domain.

The results were studied for three mesh models to investigate grid independence in the case without the VGJ ((mesh model = cell number), coarse = 1,024,128, normal = 1,922,544, fine = 3,894,000). Figure 3 investigates grid independence in the case without a jet. For this purpose, the pressure coefficient, x velocity, and Reynolds stress were considered. Figure 3b depicts the pressure coefficient on the wind tunnel floor. Further, Fig. 3b depicts velocity along the x -direction and Fig. 3c and d show $u'u'$ and $u'v'$, respectively. The graphs are suggestive of a pressure drop along the stream to the point where the top plate opens up. Then, as the plate opens, velocity decreases in the longitudinal direction, bringing the pressure back up again. Moreover, the figure shows the velocity in the x -direction at $x/L = 0.1714$ section. The figure shows the velocity along x to start from 0 at the channel floor, rising parabolically until the boundary layer $\frac{y}{\delta} = 1$, beyond which it remains constant. Further, Reynolds stresses also rapidly increase from 0 at the channel

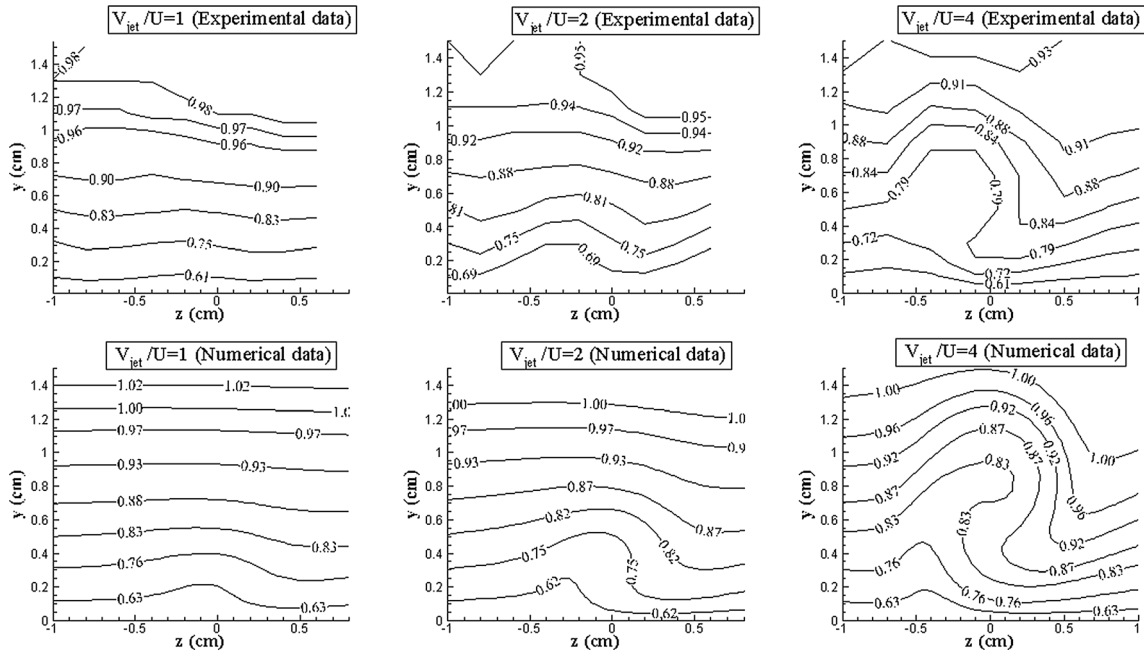


Fig. 4 Comparison of the numerical and experimental results for u/U contours for various microjet velocities at $x = 0.09$ m

floor due to steep velocity gradients. The parameters then decrease, dropping to nearly zero near the boundary layer where velocity changes are negligible. These figures show that the three models produced fairly similar results. There is a slight difference between the results from the coarse grid and those from the other two mesh densities. There was also about less than 1% discrepancy among the results in this case.

The results indicate that the three mesh densities could provide reasonable accuracy for the present problem. However, adding a pair microjet resulted in more substantial velocity variations near the boundary and led to larger errors in the case of the coarse grid. Therefore, the normal grid density was chosen for the next stages of the analysis.

The verification experiment was completed in a low-speed closed-circuit boundary layer wind tunnel. An adverse pressure gradient turbulent boundary layer with the microjets was measured. Hot-wire technique was applied to measure the flow velocities and Reynolds stresses. Similar methods were applied in other experimental researches (Budiman et al. 2016; Hasheminejad et al. 2017). Wire anemometer used is FML constant temperature anemometers operating at a resistance ratio of 1.8. The single wire probe is a DISA 55 POS probe. The cross wire probe is DOSA 55-p-51 dual sensor hot-wire probe. The probes used 2.5 μ s platinum coated tungsten wire which was copper plated and then etched for an active length to diameter ratio of 250. The data acquisition was performed with a 586 PC and National Instruments PCI-MID-16 Board (12 bit A/D).

The single wire signals were sampled at 1 kHz for 20 s giving 20,000 samples per y Position in the profiles. At each measurement position, 6000 samples from each wire of cross wire probe were acquired using the external simultaneous sample- and -hold at a frequency of 60 Hz. The boundary layer flow is well developed turbulent boundary layer. The two-axis traverse system has a resolution of 0.0032 mm in vertical direction and 0.0064 mm in spanwise direction. The spatial resolution of the hot-wire Measurements is 0.65 mm*1.0 mm (y * Z). The longitudinal pressure gradient is measured using wall taps. The static pressure data is measured by Celesco P7D diaphragm-type pressure transducer with a range of ± 0.1 psi.

According to the uncertainty analysis of Anderson and Eaton (Anderson and Eaton, 1989), the mean velocity had an uncertainty of 3% of the local streamwise velocity. The normal Reynolds stress components had an uncertainty of 5% of the local value of u'^2 . The shear stress had an uncertainty of 10% of the local value of $u'v'$.

Figure 4 compares the experimental and numerical results for a surface flow with a microjet. The comparison was made at 9 cm from the microjet by considering u/U for VRs = 1, 2, and 4, corresponding to percentage errors of 1%, 3%, and 5%, respectively. As the figure shows, there is good agreement between

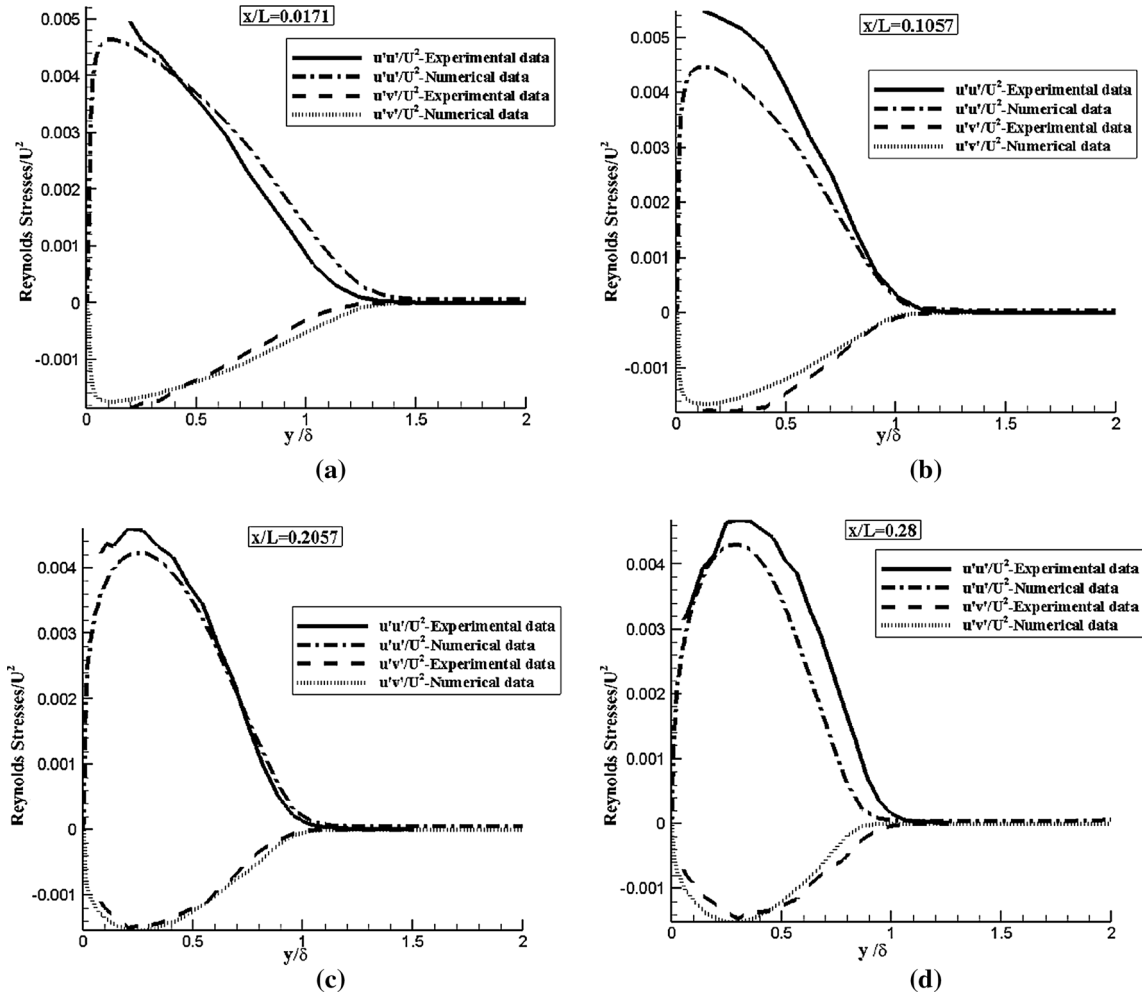


Fig. 5 Comparison of numerical and experimental Reynolds stresses $u'u'$ and $u'v'$: **a** $x/L = 0.0171$, **b** $x/L = 0.1057$ m, **c** $L = 0.2057$, and **d** $x/L = 0.28$ m (Razzaghi et al. 2021)

the experimental and numerical results. It was concluded that the numerical results could be used in further stages through the analysis process.

Figure 5 shows the numerical and experimental Reynolds stresses at different cross-sections of the turbulent boundary layer of a case with a VGJ. The results indicate that there is good agreement between the numerical and experimental values. However, there is a slight discrepancy in some cases. While many cases showed a discrepancy lower than 2% between the experimental and numerical values, the discrepancy grew to 9% for some other cases.

Figure 6 plots velocity results along the x -direction and Reynolds stress $u'u'$ at $x/L = 0.2953$ for the case with two VGJs ($d/D = 10$ and $VR = 4$). At this location, the two jet-induced vortices merge and form a stronger longitudinal vortex. The numerical solution was consistent with experimental results. The highest error in these contours corresponded to areas away from the floor. Overall, the maximum error in velocity and Reynolds stress reached around 8 and 12%, respectively. According to the obtained results, SST K- ω model has a good performance in predicting the turbulence in the flow. This model can predict maximum and minimum values of Reynolds stresses in relatively correct positions and exact values.

4 Results

In light of previous discussions, the results for $VR = 4.0$ are presented in the following. Accordingly, three cases were considered. In Case 1, d/D was 10, and VGJs were placed in a co-directional configuration. In

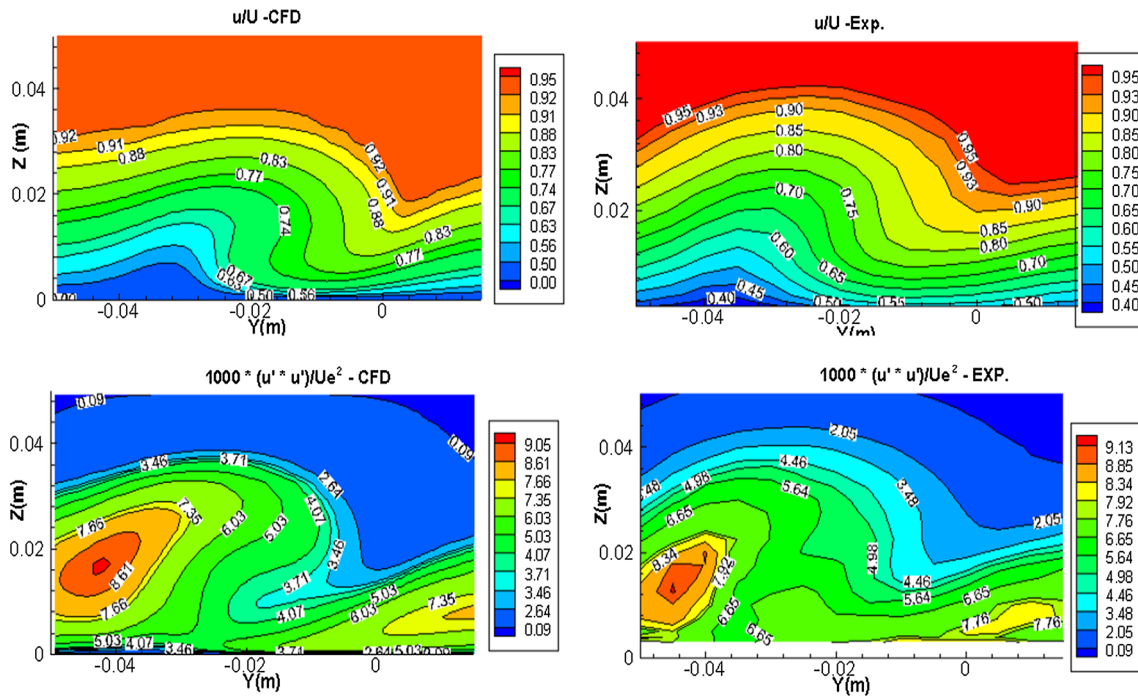


Fig. 6 Comparison of the numerical and experimental results for velocity along the x -direction and Reynolds stress $u'u'$ in the case with the VGJs pair

Case 2, d/D was 10, and VGJs were installed facing each other. In Case 3, d/D was 30, and VGJs were placed in a co-directional configuration. The velocity, Reynolds stress, and vorticity along the x -direction were studied and compared in these cases. Moreover, since the aim of using jets in pairs is to investigate longitudinal vortex amplification at the boundary layer, the results were compared to the case of a single jet.

4.1 Velocity contours

In this part, velocity contours in different sections are discussed. Figures 6, 7, and 8 show the effects of the two pairs of jets on velocity in different directions. Figure 7 reveals that by injecting the jet into the stream, the velocity is affected in all directions, in the areas where the jet affects the flow. Due to the flow in the x -direction, the accelerating effect of flow in this direction by the jet fades quickly. Also, due to the presence of a lower wall, the effect of the jet on the velocity along the y -axis is reduced more than to the z -axis. The jet effects on the boundary layer velocity perpetuate as far as $x = 0.8$ m. Figures 7, 8, and 9 show pairs of jets merging at $x = 0.04$ m, forming two strong vortices. In Case 1, the two vortices merge, forming a strong vortex at $x = 0.1$ m. The jet effects disappear at greater distances ($x = 0.8$ m), leaving the vortex to dissipate. Case 3 contours indicate that the large distance between the two VGJs affected a broader part of the stream but at the cost of the advantages of pairing two VGJs. Nonetheless, given that the vorticity of the left- and right-side vortices are slightly different in the long-range, it is anticipated that this spacing will be advantageous at higher VRs. It is also evident that the vortices get closer in Case 2. Then, pressure rises between the two VGJs, pushing them apart due to the smaller w between them. Based on velocity contours, the jet pair seems to dissipate the most energy along the z -direction. Accordingly, the velocity in this direction is lower for this pair of jets than the others. Meanwhile, velocity increased in positive x - and y -directions more than that in other jet pair configurations as the opposite jets were aimed at each other.

Figure 10 plots velocity contours and streamlines for three pairs of jets configurations at two sections ($x = 0.04$ m and $x = 0.1$ m). It is evident from Fig. 9 that, depending on the vortex direction, the momentum of the mainstream enters the boundary layer from one side of the vortex. Accordingly, the boundary layer becomes thinner in the down-wash region and thicker in the up-wash region. Based on the contours, there is no interruption in these regions in Case 3, which is almost similar to a pair of fully separated VGJs. In Case 2, since the two vortices rotate in opposite directions, the up-wash regions merge, affecting the boundary layer to a greater extent. Over time, with the pair of vortices moving apart, the up-wash effects on the

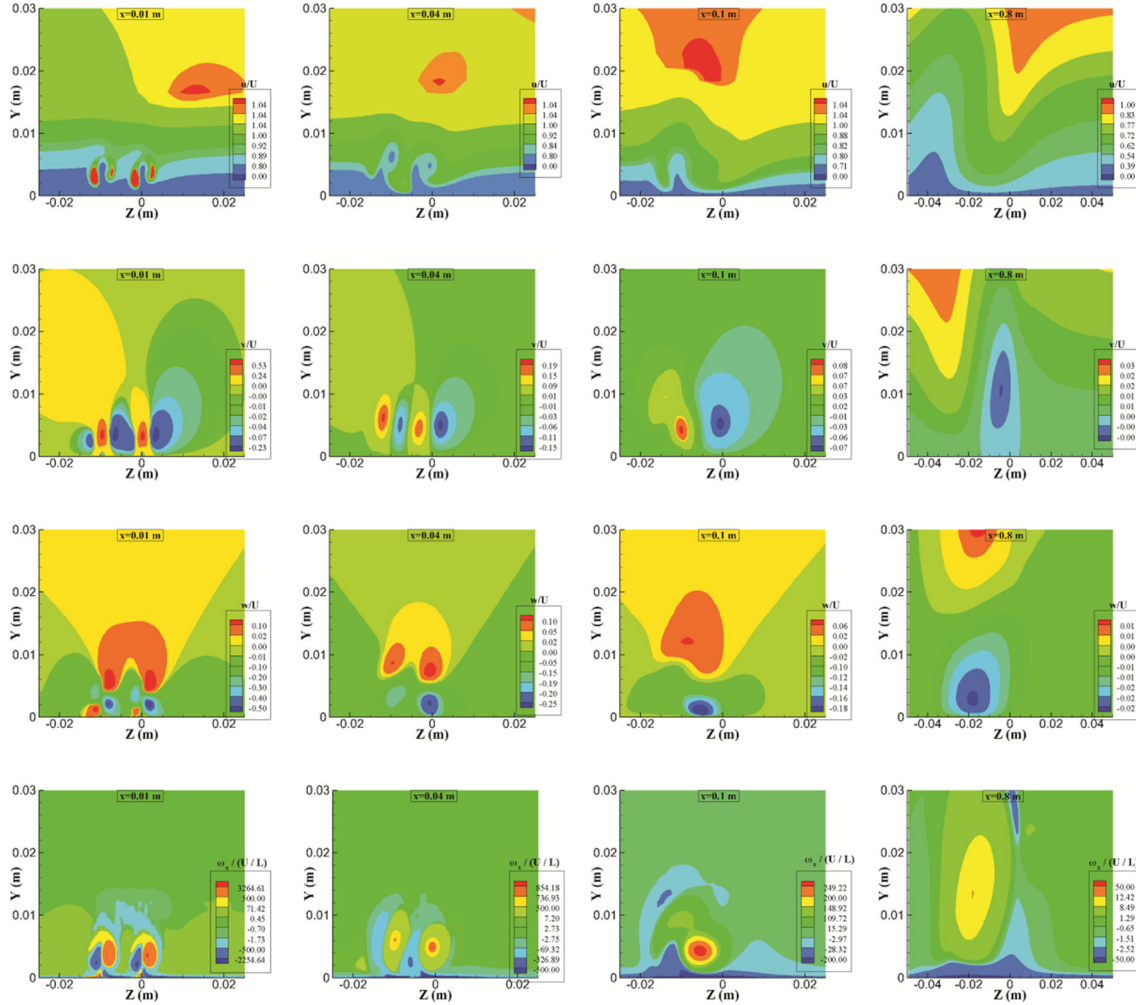


Fig. 7 Velocity contour along the x -direction for Case 1 at several flow sections

boundary layer also dwindle. Moreover, in Case 1, the appearance of two vortices at $x = 0.04$ m versus one at $x = 0.1$ m affected the boundary layer differently. For $x = 0.04$ m, the down-wash of the right-side vortex is seen reaching into the up-wash of the left-side vortex. Nonetheless, down-wash and up-wash regions can be found to the right of the right-side vortex and the left of the left-side vortex. Over time, as the two vortices merge, the region bordering the two vortices disappears gradually. Further, the overall effects of the vortex on the boundary layer exacerbate, affecting a larger part of it.

4.2 Vorticity contours

Figure 11 shows the vorticity counters in three cases for different sections. By comparing the vortices, it can be concluded that for Cases 1 and 2, the vortex remains within the boundary layer area. It is also known that the strength of vortices in Case 1 is higher than in other cases. Comparing Cases 2 and 3, it is clear that, in general, the vortices formed in Case 3 are more powerful. Also, the vortices formed in Case 2 have left the boundary layer and therefore have lost their effects in the boundary layer. Moreover, in Case 1, at $x = 0.1$ m, since the vortex merged with the left-side one from the top, the vortex was deformed and flattened.

In the following, the position and strength of vortices compared to a single jet vortex have been investigated. It is evident from Fig. 12 that in Case 1, a pair of co-VGJs are employed at $d/D = 10$, the vortex spacing gradually decreases to the point where at $x/L = 0.02$, the left-side vortex of the pair dissipates into the right-side one. Since jet velocity is much higher than the input flow velocity and given the fact that the left- and right-side vortices are, respectively, exposed to free flow and the left-side vortex, vorticity is

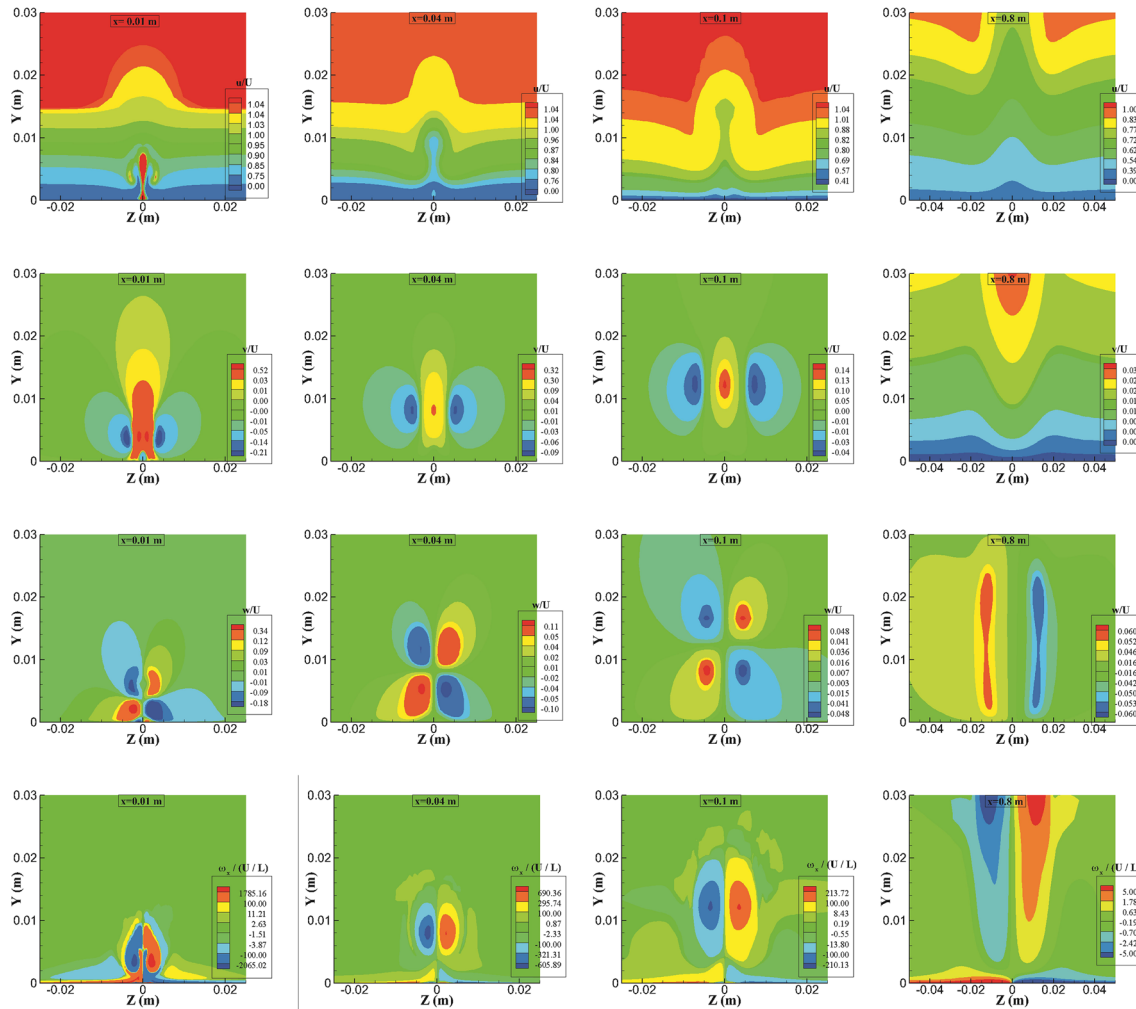


Fig. 8 Velocity contour along the x -axis for Case 2 at several flow sections

stronger on the right than on the left side. In this case, due to their direction of rotation, the right-side vortex pushed the left-side one upward. The left-side vortex gradually merges into the right-side one from the top. The strong new vortex can affect the flow to a greater extent and take longer to dissipate.

In Case 2, we put the pair of fluid jets opposite each other; after getting closer to the point of contact, the vortices move away from the floor and—almost linearly—each other, driven by their rotation directions. It is also evident that this configuration results in slightly lower vorticity than the one with a single VGJ. Further, the vortices move considerably away from the surface and may even leave through the boundary layer.

In Case 3, the ratios of the jet pair’s vorticity and distance to the channel floor to those of the single jet were approximately 1. That is to say, the two VGJs did not have a considerable impact on each other. In this case, the two jets actually work independently. Nonetheless, the mutual influence of the two jets is evident, which has led to slightly different results for the right- and left-side VGJs. The differences between results increased with x/L rising. The differences between the long-range vorticity results of the two VGJs remained around 10%.

Overall, the best results were achieved in Case 1. In this case, long-range vorticity was found to be more than 80% higher with a pair of jets than in the single-VGJ case. In this light, it is concluded that Case 1 can produce better results than other cases and the single jet configuration. The advantages of using a pair of jets appear at high-velocity levels. The results also suggest that this choice does not push the vortex out of the boundary layer.

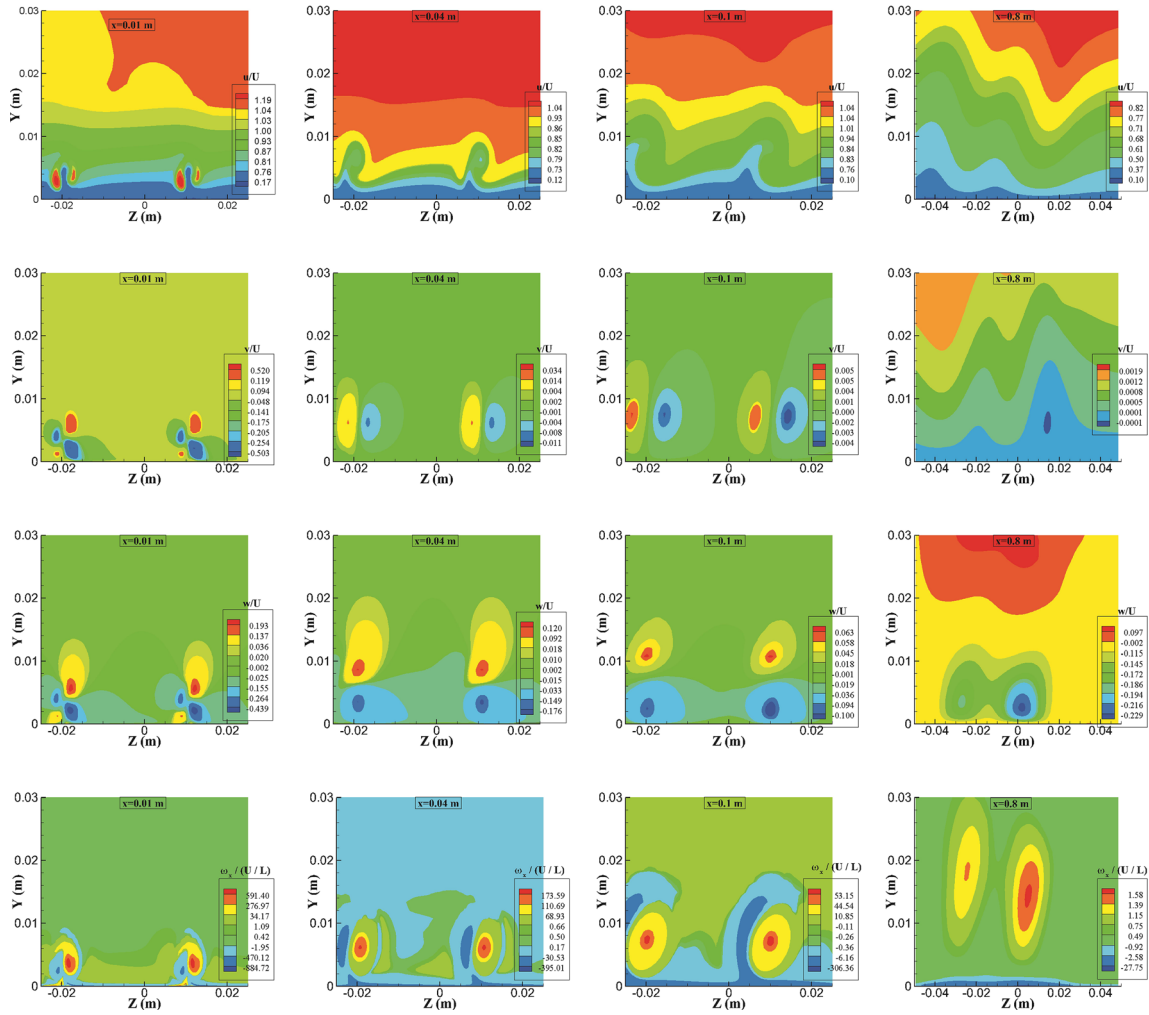


Fig. 9 Velocity contour along the x -axis for Case 3 at several flow sections

4.3 Reynolds stress contours

Figures 13, 14, and 15 plots Reynolds stress contours at different sections. It is evident that further away from the micro-jet, stresses diminish at the boundary layer. Further, $u'u'$ is found to be larger than $u'v'$ and $u'w'$. The reason can be attributed to free flow along the x -direction and the channel opening along the y -direction, pushing the stream in that direction. Moreover, $u'w'$ and $u'v'$ can be seen to change more than $u'u'$ in the boundary layer. This outcome is, in fact, a result of free flow and its dominant effect on the $u'u'$ Reynolds stress. Also, the VGJ effects on $u'v'$ at the boundary layer diminished more rapidly due to flow variations in the aftermath of the channel opening and flow along the y -axis. Meanwhile, the VGJ was the only factor driving the flow along the z -direction; therefore, the effects were manifested in the boundary layer more than anywhere else. Furthermore, as demonstrated by Case 2 contours, Reynolds stresses are symmetric with respect to $r = 0$. The maximum Reynolds stress moves away from the floor more rapidly than in Cases 1 and 3 configurations. It is also evident that the pair of jets did not have a considerable mutual effect in terms of Reynolds stress in Case 3. It is also evident from the contours that $u'u'$ was higher around the VGJ in Case 2. Since, in this case, the two jets are facing each other, velocity changes are the most drastic near the VGJ, which translates to a higher Reynolds stress. Nonetheless, Reynolds stress levels in the three VGJ configurations become similar further away from the VGJ.

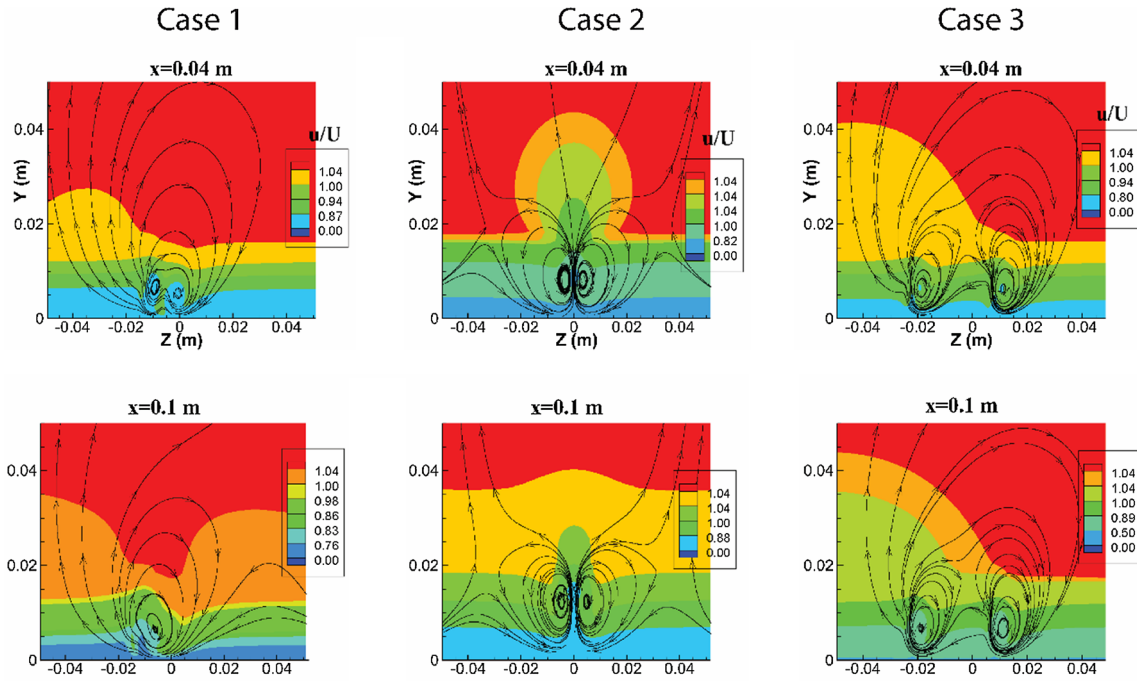


Fig. 10 Contours showing vortex effects on the longitudinal velocity at the boundary layer in different cases and different sections

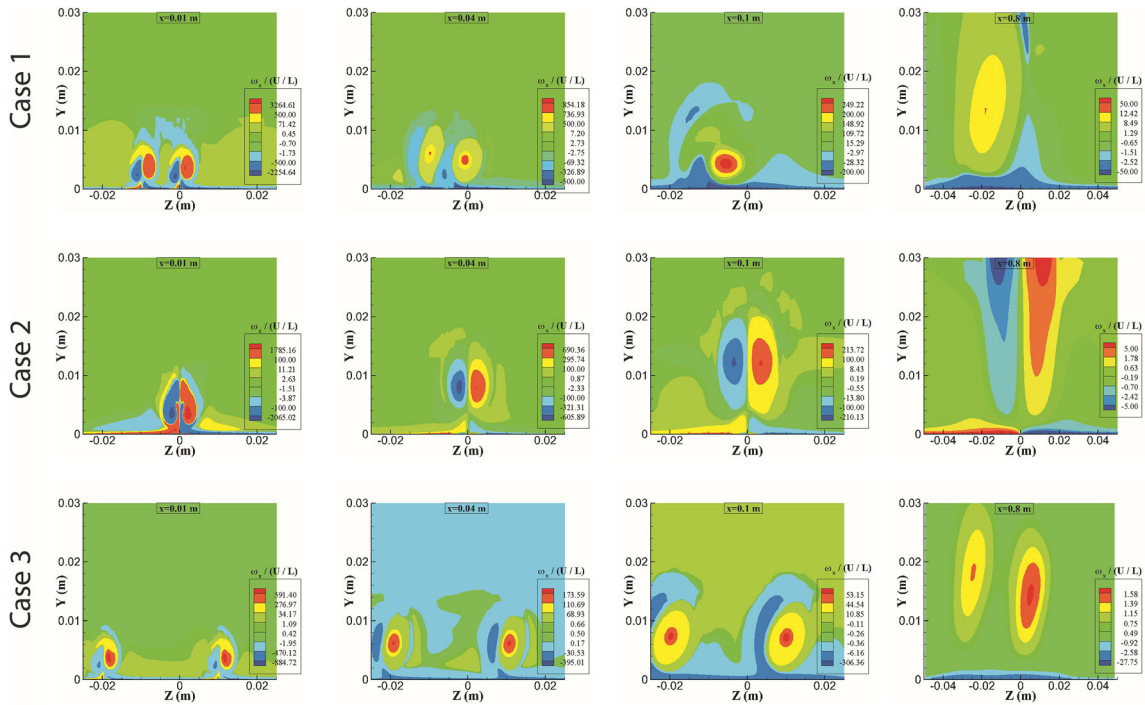


Fig. 11 Vorticity contour along the x -direction for different cases at several flow sections

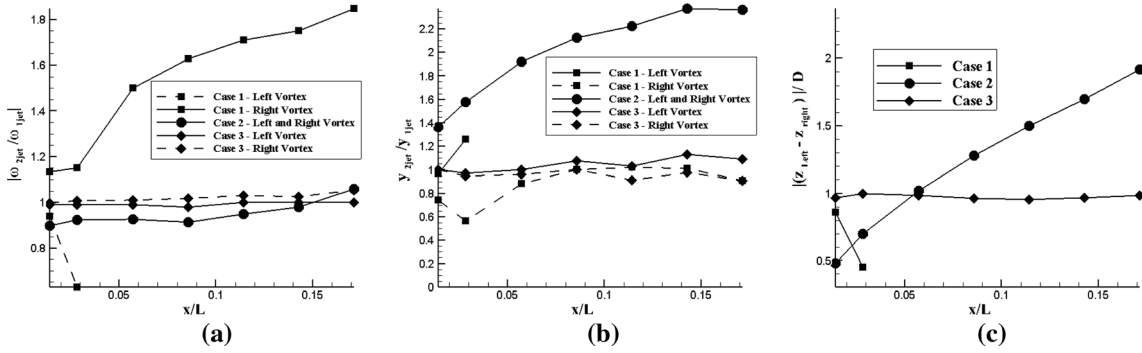


Fig. 12 Comparison of three different cases results with the single jet one. **a** The ratio of vorticity, **b** vertical location of vortices, and **c** center-to-center distance of vortices

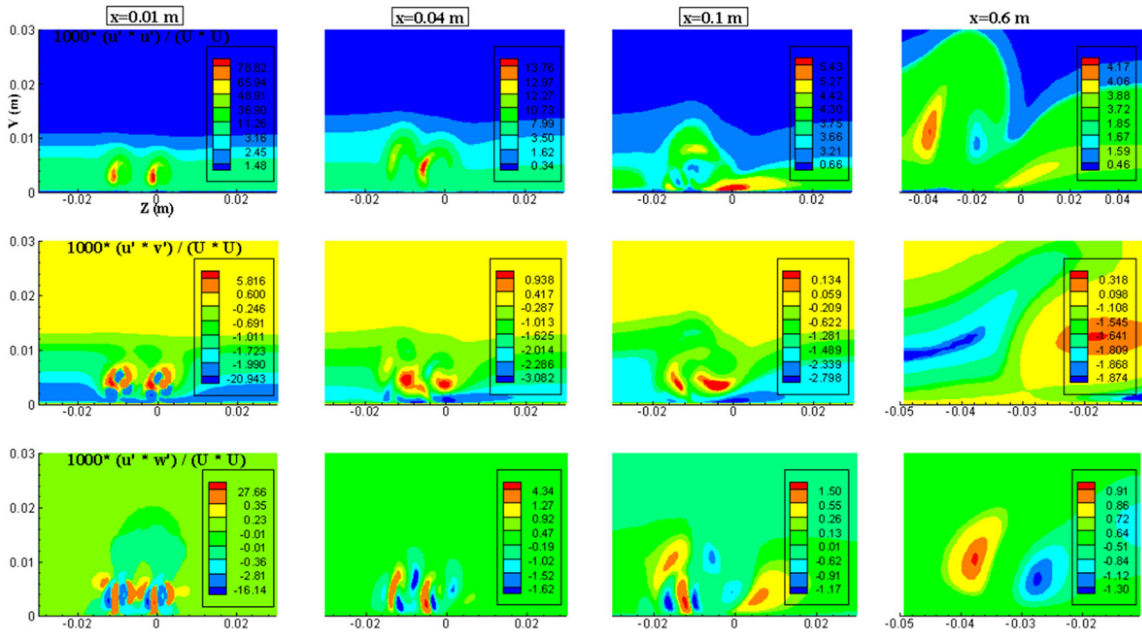


Fig. 13 $u'u'$, $u'v'$, and $u'w'$ stress contours for Case 1

4.4 Boundary layer variations and static pressure

Figure 16 presents the boundary layer results for configurations without a VGJ and with a pair of them at four different sections. It is evident from the results that the boundary layer further expands the closer the stream moves to the end of the plate. Figure 15 indicates that the boundary layer thickness was reduced in the down-wash region due to the momentum exerted on the boundary layer by the free flow. In Case 2, due to the build-up of energy between the two vortices, the boundary layer exhibits more growth. Further, both down-wash and up-wash regions develop for $d/D = 3$. Nonetheless, in the right-side vortex's down-wash, the boundary layer was narrowed more than that on the left side. It is also evident that in Case 1, down-wash and up-wash regions disappear due to vortex interferences. Moreover, compared to the boundary layer without jets, adding the VGJs caused the boundary layer to form partly above where it would in the VGJ-free case and partly below that. Regardless, Fig. 15 shows that in Case 1, particularly around the VGJ, the boundary layer develops lower than it would in conditions without jets.

Figure 17 depicts static pressure over the plate in the VGJ-free and the other three configurations. Based on the studied geometry, pressure decreased along the channel. By considering the region where the height of channel increases, velocity decreases along the stream thus pressure increases. The back-pressure increased linearly. As illustrated in Fig. 16, the pair of jets pushed back the back-pressure rise. Further away from the jet, the effects of geometry and the mainstream dominate pressure effects, resulting in matching

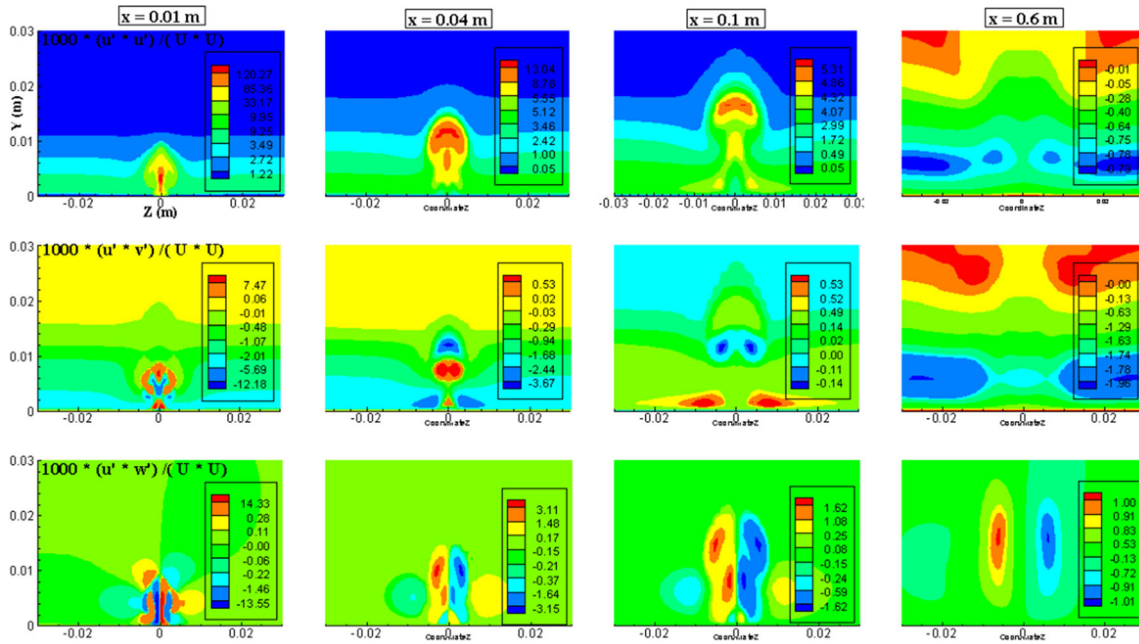


Fig. 14 $u'u'$, $u'v'$, and $u'w'$ stress contours for Case 2

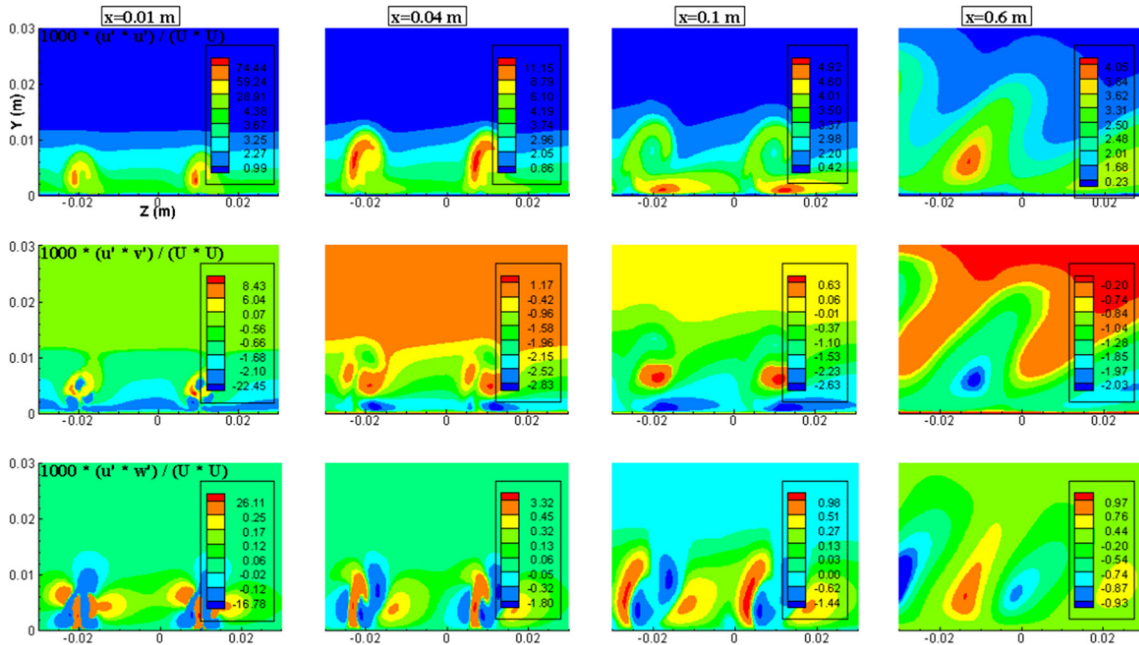


Fig. 15 $u'u'$, $u'v'$, and $u'w'$ stress contours for Case 3

graphs. Nonetheless, until 30 cm after jet injection, the pair of jets produces a lower static pressure in compare without VGJ.

4.5 Streamlines of vortices merging in Case 1

Figure 18 plots the streamlines for Case 1. Accordingly, vortex formation and interaction were investigated at different sections near the bottom wall. It is evident from the figure that, first, a counter-rotating pair of vortices form. The left-side vortex, which receives a smaller momentum due to the microjet, is forced closer

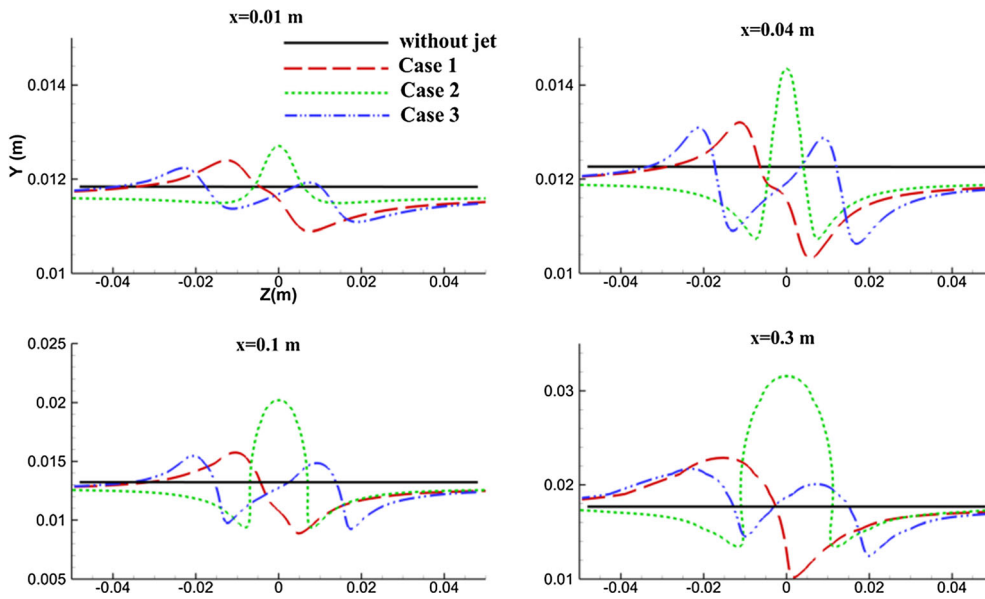


Fig. 16 Boundary layer variations are caused by VGJ pairs compared to the VGJ-free configuration

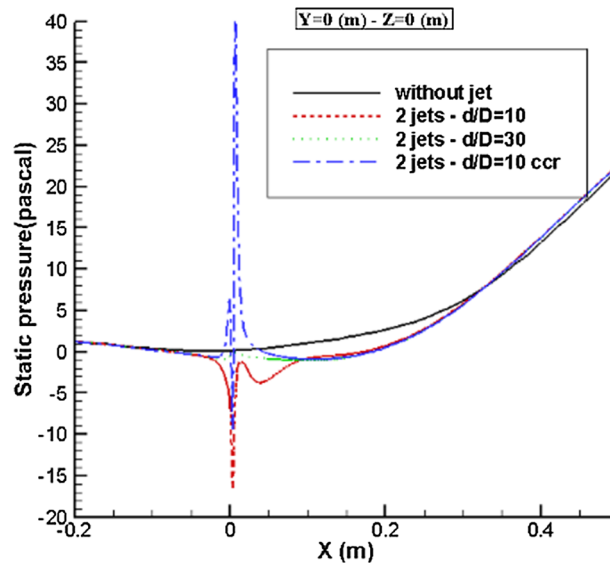


Fig. 17 Static pressure contours for Cases 1 through 3 and the VGJ-free configuration

to the surface by the stronger vortex. The vortex dissipates as it approaches the surface, weakening it until elimination. The distribution of strength and vorticity between the counter-rotating vortices drives the pair unevenly toward unification. As the weaker vortex of the pair dissipates, it wraps around the dominant vortex (Johansen 2005; Iuso et al. 2018). According to the figure, the dominant vortex resulting from each microjet formed around $x = 0.03$ m. Based on what was discussed, between the two dominant co-directional vortices, the one on the right is stronger. Therefore, the left-side vortex merged into the right-side one. The figure indicates that the single dominant vortex formed at $x = 0.08$ m. The vortex diminishes and ascends as it advances along the stream. Finally, the vorticity decreases to the point where the vortex nearly dissipates around $x = 0.08$. Further, the figure suggests that, depending on the jet orientation, the vortex rotates toward the z -axis as it moves along the stream.

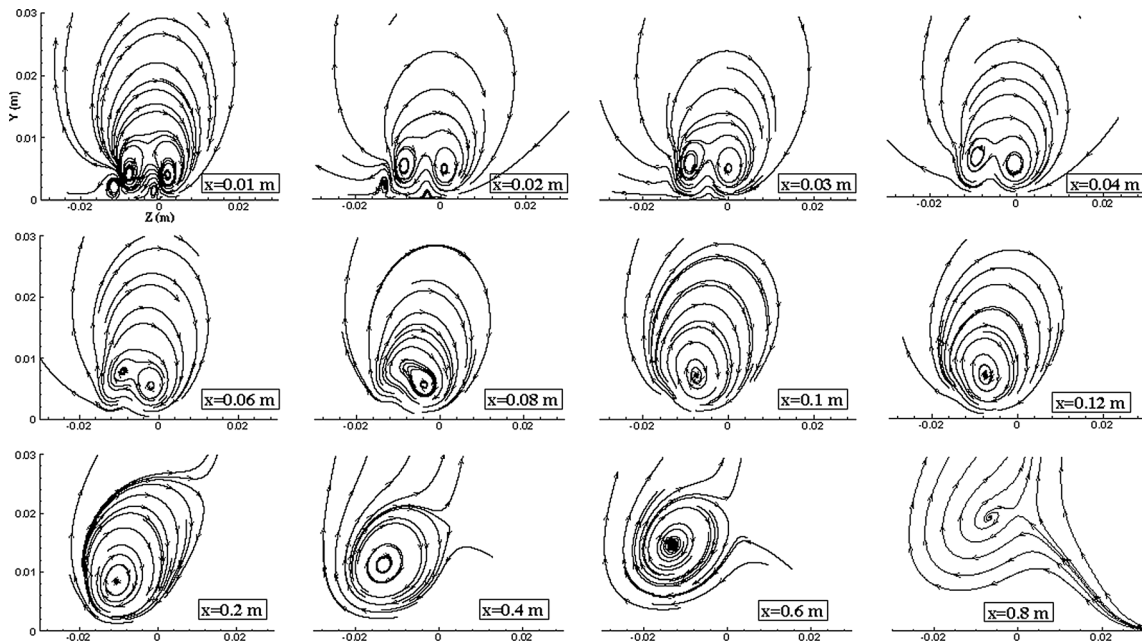


Fig. 18 Streamline contours for Case 1 at different sections, illustrating merging

5 Conclusion

The present study investigates the effects of the orientation and spacing between a pair of VGJs on the turbulent boundary layer in a flow over a plate. For this purpose, three cases were considered and studied at $VR = 4$. The analysis was carried out considering $\alpha = 30^\circ$ and $\beta = -60^\circ$ and 60° . The analysis produced the following results:

- (1) The vortices merged only in Case 1. The strong new vortex can affect the flow to a greater extent and take longer to dissipate. This stronger vortex remained almost entirely in the boundary layer. Further, the vortex affected the boundary layer by reducing its thickness in the down-wash and expanding it in the up-wash. However, the thinning was more considerable than the expansion.
- (2) The vortices merged only in Case 1. The strong new vortex can affect the flow to a greater extent and take longer to dissipate. This stronger vortex remained almost entirely in the boundary layer. Further, the vortex affected the boundary layer by reducing its thickness in the down-wash and expanding it in the up-wash. However, the thinning was more considerable than the expansion.
- (3) In Case 2, the two vortices rotated in opposite directions but symmetrically, moving closer and backing away again. Because the two jets were facing each other, velocity changes were more drastic between the two vortices. Accordingly, Reynolds stresses were more considerable in the vicinity of the VGJs in this case. Since vortices moved considerably away from the floor in Case 2, the maximum Reynolds stress took place outside the boundary layer.
- (4) In Case 3, the two vortices did not yield any effect on each other and produced similar results. The results showed that the long-range difference between the two vortices' intensity reached nearly 10% due to their mutual effects.
- (5) Integration of a pair of jets has affected the pressure on the channel floor. Besides the effects of the VGJ's orientation on the pressure, adding the pair of jets has successfully pushed the pressure build-up due to distance from the top plate by nearly 30 cm.

Funding This project is supported by National Natural Science Foundation of China (Grant No. 51575279).

References

- Alimi A, Wünsch O (2018) Numerical investigation of steady and harmonic vortex generator jets flow separation control. *Fluids* 3(4):94
- Anderson JD (2001) Introduction to the fundamental principles and equations of viscous flow. *Fundamentals of aerodynamics*, 3rd edn. McGraw-Hill, New York, pp 713–744
- Anderson SD, Eaton JK (1989) Reynolds stress development in pressure-driven three-dimensional turbulent boundary layers. *J Fluid Mech* 202:263–294
- Beresh SJ, Henfling JF, Spillers RW, Pruett B (2018) Influence of the fluctuating velocity field on the surface pressures in a jet/fin interaction. *J Spacecr Rocket* 55(5):1098–1110
- Budiman A et al (2016) Development of pre-set counter-rotating streamwise vortices in wavy channel. *Exp Therm Fluid Sci* 71:77–85
- Davidson L (2015) “An introduction to turbulence models.”
- Raman A (2016) “Numerical investigation of vortex generators and jet in cross-flow enhancements.” PhD diss
- Feng Y-Y, Song Y-P, Breidenthal RE (2018) Model of the trajectory of an inclined jet in incompressible crossflow. *AIAA J* 56(2):458–464
- Godard G, Stanislas M (2006) Control of a decelerating boundary layer. Part 3: optimization of round jets vortex generators. *Aerosp Sci Technol* 10(6):455–464
- Hasheminejad S et al (2017) Development of streamwise counter-rotating vortices in flat plate boundary layer pre-set by leading edge patterns. *Exp Therm Fluid Sci* 86:168–179
- Iuso G, Vigevano L, Scialabba G (2018) “Effects of injector geometry in air-jet vortex-generator flow control.” PhD diss., Master Thesis, Institute of Aerodynamics, 2018. Google Scholar, 2018
- Johansen CT (2005) “Numerical simulations of turbulent flows.” PhD diss., Carleton University
- Lefebvre AM (2015) Investigation of co-flow jet flow control and its applications. University of Miami
- Liu Y, Zhang H, Liu P (2019) Flow control in supersonic flow field based on micro jets. *Adv Mech Eng* 11(1):1687814018821526
- Masumi Y, Nikseresht AH (2017) Comparison of numerical solution and semi-empirical formulas to predict the effects of important design parameters on porpoising region of a planing vessel. *Appl Ocean Res* 68:228–236
- McCurdy, W “Investigation of boundary layer control of an NACA 16–325 airfoil by means of vortex generators.” United Aircraft Corp, Research Department, Rept. M-15038–3 (3 December 1948). Print (1948)
- Ortmanns J, Kähler CJ (2007) The effect of a single vortex generator jet on the characteristics of a turbulent boundary layer. *Int J Heat Fluid Flow* 28(6):1302–1311
- Pearcey HH (1961) Shock induced separation and its prevention. *Bound Layer Flow Control* 2:1170–1344
- PourRazzaghi MJ, Xu C (2020) Numerical study of minute vortex generator jets in a turbulent boundary layer. *J Phys Conf Series* 1507(8):082011
- Razzaghi P, Javad M, Cheng Xu, Liu Y, Masoumi Y (2021) The effects of minute vortex generator jet in a turbulent boundary layer with adverse pressure gradient. *Sci Prog* 104(2):00368504211023294
- Rixon GS, Johari H (2003) Development of a steady vortex generator jet in a turbulent boundary layer. *J Fluids Eng* 125(6):1006–1015
- Von Stillfried F, Wallin S, Johansson AV, Casper M, Ortmanns J (2012) Evaluation and parameterization of round vortex generator jet experiments for flow control. *AIAA J* 50(11):2508–2524
- Wallis RA (1952) The use of air jets for boundary layer control. AERONAUTICAL RESEARCH LABS MELBOURNE (AUSTRALIA)
- Wang S, Ghaemi S (2019) Effect of vane sweep angle on vortex generator wake. *Exp Fluids* 60(1):1–16
- White FM, Majdalani J (2006) *Viscous fluid flow*, vol 3. McGraw-Hill, New York